

OPEN ACCESS

Repository of the Max Delbrück Center for Molecular Medicine (MDC) in the Helmholtz Association

<https://edoc.mdc-berlin.de/17035/>

Millimeter Spatial Resolution In Vivo Sodium MRI of the Human Eye at 7.0 Tesla Using a Dedicated Radiofrequency Transceiver Array

Wenz D., Kuehne A., Huelnhagen T., Nagel A.M., Waiczies H., Weinberger O., Oezerdem C., Stachs O., Langner S., Seeliger E., Flemming B., Hodge R., Niendorf T.

This is the final version of the accepted manuscript, which was published in final edited form in:

Magnetic Resonance in Medicine
2018 AUG; 80(2): 672-684, 2018
2018 JAN 12 (first published online)
doi: <https://doi.org/10.1002/mrm.27053>

Publisher: [Wiley](#)

Publisher's Notice

This is the peer reviewed version of the following article:

Wenz D., Kuehne A., Huelnhagen T., Nagel A.M., Waiczies H., Weinberger O., Oezerdem C., Stachs O., Langner S., Seeliger E., Flemming B., Hodge R., Niendorf T. Millimeter spatial resolution in vivo sodium MRI of the human eye at 7 T using a dedicated radiofrequency transceiver array. *Magn Reson Med* 80(2): 672-684, 2018

which has been published in final form at <https://doi.org/10.1002/mrm.27053>. This article may be used for non-commercial purposes in accordance with [Wiley Terms and Conditions for Self-Archiving](#).

Copyright © 2018 International Society for Magnetic Resonance in Medicine

Millimeter Spatial Resolution In Vivo Sodium MRI of the Human Eye at 7.0 Tesla Using a Dedicated Radiofrequency Transceiver Array

Daniel Wenz¹, Andre Kuehne², Till Huelnhagen¹, Armin M. Nagel^{3,4}, Helmar Waiczies², Oliver Weinberger¹, Celal Oezerdem¹, Oliver Stachs⁵, Soenke Langner⁶, Erdmann Seeliger⁷, Bert Flemming⁷, Russell Hodge¹, Thoralf Niendorf^{1,2}

¹ Berlin Ultrahigh Field Facility (B.U.F.F.), Max Delbrueck Center for Molecular Medicine in the Helmholtz Association, Berlin Germany

² MRI.TOOLS GmbH, Berlin, Germany

³ Institute of Radiology, University Hospital Erlangen, Erlangen, Germany

⁴ Division of Medical Physics in Radiology, German Cancer Research Centre (DKFZ), Heidelberg, Germany

⁵ Department of Ophthalmology, University of Rostock, Rostock, Germany

⁶ Institute for Diagnostic Radiology and Neuroradiology, University Medicine Greifswald, Greifswald, Germany

⁷ Institute of Physiology, Charité University Medicine, Berlin, Germany

Correspondence to: Prof. Dr. Thoralf Niendorf
Berlin Ultrahigh Field Facility (B.U.F.F.)
Max-Delbrueck-Center for Molecular Medicine
Robert-Roessle-Strasse 10
13125 Berlin
Germany

phone: +49 30 9406 4505
fax: +49 30 9406 49178
e-mail: thoralf.niendorf@mdc-berlin.de

Running title: Millimeter Spatial Resolution In Vivo Sodium MRI of the Human Eye at 7.0 Tesla

Key words: sodium, eye, transceiver array, 7.0 T

Word count: 4416

Abstract

Purpose:

The aim of this study was to achieve millimeter spatial resolution sodium (^{23}Na) in vivo magnetic resonance imaging of the human eye at 7.0 Tesla using a dedicated six-channel transceiver array. We present a detailed description of the RF coil design along with electromagnetic field (EMF) and specific absorption ratio (SAR) simulations, data validation and in vivo application.

Methods:

EMF and SAR simulations were performed. Transmit field uniformity was optimized by using a multi-objective genetic algorithm. Transmit field mapping was conducted employing a phase-sensitive method. An in vivo feasibility study was carried out with a 3D density-adapted projection reconstruction imaging technique.

Results:

Measured transmit field distribution agrees well with the one obtained from simulations. SAR simulations confirm that the RF coil is safe for clinical use. Our RF coil is light and conforms to an average human head. High spatial resolution (nominal 1.4 and 1.0 mm isotropic) sodium in vivo images of the human eye were acquired within scan times suitable for clinical applications (~ 10 minutes).

Conclusions:

Three most important eye compartments in the context of sodium physiology were clearly delineated in all of the images: the vitreous humor, the aqueous humor and the lens. Our results provided encouragement for further clinical studies. The implications for research into eye diseases including ocular melanoma, cataract and glaucoma are discussed.

Introduction

A growing number of reports refer to proton MRI of the human eye and orbit in vivo at ultrahigh magnetic fields ($B_0 \geq 7.0$ Tesla). Recent studies include high-spatial resolution imaging of the bulbus oculi and its surrounding structures (1,2), the optic nerve (3,4) and retrobulbar vessels (5). Ultrahigh field (UHF) MRI can also help to differentiate eye tumors such as uveal melanomas from healthy tissues with high fidelity (6-9). Diffusion-weighted ophthalmic imaging free of geometric distortions at 7.0 T provides value for diagnosis and treatment of intraocular masses (10). Yet the potential of UHF-MRI in diagnosing ocular disorders remains to be further utilized. Sodium (^{23}Na) imaging could be complementary to proton MRI in this context, because it provides a different type of diagnostic information which is more closely related to tissue physiology.

Sodium ions play a key role in various physiological processes in the eye (11). They are an important component of the vitreous humor (VH). The active transport of sodium ions is a driving force in the formation of the aqueous humor (AH) and is essential for maintaining the hydration status and thus the transparency of the cornea (12). It maintains a specific Na^+/K^+ gradient between the lens and VH and is also the basis for the movement of water and lactate in the retina from the retinal side to the blood. These crucial functions suggest that probing tissue sodium concentration (TSC) in the eye through MRI would add a very useful new dimension to our understanding of ocular disorders.

This strategy would likely be useful in the various types of cataracts and glaucomas which remain two main causes of blindness and currently affect almost 30 million people in the US (13,14). A number of studies have found increases in Na^+ concentration in cataractous lenses (15,16). Diminished Na^+ concentration in the AH (17) probably contributes to the pathophysiology of bilateral acute angle closure glaucoma (18).

MRI studies have confirmed that TSC is higher in malignant brain (19) and breast (20) tissue than in their healthy counterparts, suggesting that the same may be true in eye tumors which are detected in 2.500 patients in the US every year (21). These findings indicate that sodium quantification in the eye may be a valuable aid not only in diagnosis, but also in follow-up after proton beam therapy for eye tumors (22).

UHF-MRI is accompanied by an inherent improvement in the signal-to-noise ratio (SNR) that opens the door on visualizing ^{23}Na , the nucleus that yields the second strongest NMR signal, and the physiological processes in which it is involved. Whole-body sodium imaging at

3.0 T has shown that relative SNR in the eye is second highest among all tissues (23). While ^{23}Na MRI has already been performed at 7.0 T for tissues including the brain (24), kidneys (25), heart (26,27) and skin (28), there has not yet been a report of sodium imaging of the human eye in vivo at ultra-high field or even at lower field strengths. A few ex vivo studies have been conducted on enucleated bovine and human eyes (29-32). The only in vivo data can be found by coincidence in publications on sodium imaging of the human brain at different field strengths: 1.5 T (33), 3.0 T (34), 7.0 T (24), 4.7 T (35), 9.4 T (36). One must notice that suboptimal RF coil set-ups in the context of eye imaging were used for these investigations. Even though the main observation from these studies is that ^{23}Na signal from the eyes, which is prominent in particular slices of the human head, essentially dominates any other ^{23}Na signal from the brain.

The aim of this study is to achieve millimeter isotropic spatial-resolution ^{23}Na imaging of the human eye in vivo at 7.0 T and to determine its value in understanding and diagnosing diseases of this intricate tissue. For this purpose we propose a six-channel transceiver RF array that covers both eyes and is customized for sodium imaging of this tissue at 7.0 T.

Here a detailed description of the RF coil design is presented, along with results from electromagnetic field (EMF) and specific absorption ratio (SAR) simulations. Phantom experiments were conducted to validate the EMF simulations and to carefully assess the performance of the proposed transceiver array. The RF coil performance for sodium imaging of the human eye is demonstrated in vivo in an initial feasibility study. The merits and limitations of the proposed transceiver array are discussed, along with a consideration of the implications of the approach for clinical ^{23}Na ophthalmic MRI at 7.0 T.

Methods

RF Coil Design

The proposed RF coil array consists of six loop-elements and is symmetrically divided into two sections. Each section is composed of three loop-elements which were angled to each other in order to conform to the anterior part of an average human head as demonstrated in Figure 1. The size of a single element (36 x 71 mm) was chosen to achieve sufficient RF penetration depth (37) for eye imaging. The shape and the surface area of an average human head limit the number of elements per eye. Applying more than three elements per eye does not contribute to the improvement of the RF coil's performance, because they would be already too far from the region of interest. Two more elements (one per eye) could be added from the top, but they would couple strongly with all of the other loops. Offsetting the extra coupling would require more decoupling circuits (resulting in increased losses) so that the total weight would increase along with impairment in the patient comfort without any gain in the performance. The arrangement of element 1 (or element 4) versus element 2 (or element 5) was obtained by applying an inclination angle of 151° . In order to arrange element 2 (or element 5) versus element 3 (or element 4), an angle of 161° was applied. The six-channel array is made up of four loops of rectangular shape (elements 1, 2, 4, 5) and two of polygonal shape (elements 3 and 6). The polygonal loops are designed to fit the space around the nose in a way that permits bilateral vision through them (Figure 2a-c). To achieve a sufficient radio frequency field (RF) penetration depth, the height of a single loop was set at 71 mm and its width at 36 mm. The width of the conductor was 10 mm. The elements designed in this way were manufactured from 36 μm copper on a 0.5 mm FR-4 substrate using a CNC machine (ProtoMat, LPKF Laser & Electronics AG, Garbsen, Germany). Adjacent loops (elements 1/2; elements 2/3; elements 6/5 and elements 5/4), which share common conductor, were capacitively decoupled. Non-adjacent loops (elements 1/3; elements 6/4) were inductively decoupled, as were the two loops around the nose (elements 3/6). The capacitive decoupling was achieved using chip ceramic capacitors (American Technical Ceramics Inc, Huntington Station, NY, USA) along with trimmer capacitors (Voltronics Inc, MD, USA). Inductive decoupling was accomplished using inductors (inner diameter – 6 mm, wire thickness – 1 mm) covered by a thin layer of insulation. In order to facilitate inductive decoupling between non-adjacent elements, two small pieces of coaxial cable were used to close the circuits as illustrated in Figure 1. Cable traps were placed 10 cm away

from the coil to eliminate common mode currents (Figure 2a). They were built from a wound cable and a capacitor which was soldered to the outer shield of the cable. The coil casing was designed by using Autodesk Inventor Professional 2013 (Autodesk Inc, San Rafael, CA), and was constructed from ABS material using 3D printer (BST 1200es; Dimension Inc, Eden Prairie, MN). The dimensions of the proposed array conform to the phantom used for validation of the simulations (Figure 2b) and to an average human head (Figure 2c).

Numerical EMF Simulations

Electromagnetic field (EMF) and specific absorption rate (SAR) simulations were performed using the Finite Integration Technique (FIT) of CST Studio Suite 2015 (CST AG, Darmstadt, Germany) with the human voxel models: Duke (male) and Ella (female) from the Virtual Family (38). The electrical properties of all tissues were altered according to the IT'IS database (IT'IS, Zurich Switzerland). The coil casing was designed with Autodesk Inventor Professional 2013, which was imported into the CST Studio Suite and included in the EMF and SAR simulations. The results of the simulations were exported from the CST Studio Suite into the Advanced Design System (ADS) (Keysight EEsof EDA, CA, US). In ADS, each loop element of the coil array was tuned to the resonant frequency of 78.6 MHz and matched to the impedance of 50 Ω . Coupling between all of the elements was analyzed and capacitive-inductive circuits were designed to reduce it. Capacitors and inductors used in simulations were modeled with additional resistances, which represented losses typical for lumped elements and losses inherent to soldering joints (37,39). The final circuit designed in ADS was reproduced in the same way in the schematic view in CST. This set-up was used to calculate the transmit field (B_1^+) of the six-channel array and SAR distribution in the human voxel models Duke and Ella. The input power was adjusted to meet the regulations provided by the IEC guideline International Electrotechnical Commission (IEC) 60601-2-33 Ed.3.

Bench Evaluation

Bench measurements were performed using an 8-channel vector network analyzer (ZVT 8; Rohde & Schwarz, Memmingen, Germany). Full sets of S-Parameters were measured for various loading conditions including nine volunteers (BMI: 20.1-27.1 kg/m², average BMI = 23.2 kg/m²; age: 26-33 years, average age = 29.5 years). S-Matrices were measured, exported from the network analyzer and analyzed in Matlab (The MathWorks, Natick, MA, USA). The whole RF

chain (RF power splitter, transmit/receive (T/R) interface, adapters, phase cables and T/R switch driver) and its inevitable losses were also measured with the network analyzer. In order to approach the real performance of the coil, this data was exported as a separate S-Matrix and included in later EMF simulations.

MR Hardware

Phantom and human imaging studies were conducted on a 7.0-T whole-body system (Magnetom, Siemens Healthcare, Erlangen, Germany), equipped with a gradient system that supported a slew rate of 170 mT/m/ms, a maximum gradient strength of 38 mT/m. For RF transmission a single-channel RF amplifier ($P_{\max} = 8$ kW, Stolberg HF-Technik AG, Stolberg-Vicht, Germany) was applied. The single channel RF signal was split into six channels using a Wilkinson power divider shown in Figure 2d. All of the outputs provided signals of equal amplitude and phase and were connected via phase cables to a multipurpose interface box (MRI.TOOLS GmbH, Berlin, Germany) (Figure 2e). The multipurpose interface box consists of 16 transmit/receive switches (Stark Contrasts, Erlangen, Germany): 8 for proton (^1H) and 8 for sodium (^{23}Na) resonant frequency at 7.0 T along with integrated low-noise preamplifiers (Stark Contrasts, Erlangen, Germany). Proton MRI was performed using a volume coil (Siemens, Erlangen, Germany; Figure 2f) which is a circularly polarized birdcage configuration (inner diameter = 34 cm).

Transmit Field Optimization

In order to achieve higher transmit field (B_1^+) homogeneity in the target region, B_1^+ optimization was performed. For this purpose, the electromagnetic properties of the human voxel model tissues were extracted from CST, together with the mesh data and the B_1^+ fields of all the individual coil's elements. Secondly, a mask, which contained all of the tissues belonging to the eyes (vitreous humor, sclera, cornea and lens), was defined and used in further steps of the optimization. The mask was also isotropically enlarged (sphere's radius = 6 mm) and further modified using radially restricted (hemisphere's radius = 6 mm) morphological dilation. A multi-objective genetic algorithm (40) implemented in Matlab was used to optimize the B_1^+ field distribution within the extended mask. The optimization result was a trade-off between B_1^+ homogeneity and B_1^+ efficiency defined as: $B_1^+/\sqrt{\text{SAR}}$. Furthermore, both eyes were treated independently during optimization, and an additional constraint enforcing similar B_1^+ field

magnitude and homogeneity in both eyes was used. The resulting B_1^+ was calculated by superimposing the field of each channel with different phase. For the experiment we used one phase setting here called the phase-optimized setting (PO). It was achieved by incorporating coaxial cables for each loop element into the power splitting network.

Phantom Experiments

A cylindrical phantom was designed and built to compare simulated and measured B_1^+ distribution for the phase-optimized setting (PO). The phantom (radius = 70 mm; length = 250 mm; permittivity $\epsilon_r = 81$, conductivity $\sigma = 0.97$ S/m) was filled with water solution containing NaCl (130 mmol/l – a concentration similar to that in the human eye) and CuSO_4 (Figure 2b). B_1^+ mapping was conducted using a phase-sensitive method (41) which was incorporated into a density adapted 3D projection reconstruction imaging technique (3D-DAPR) (42).

Volunteer Study

For the in vivo feasibility study, subjects were included after due approval by the local ethical committee (registration number DE/CA73/5550/09, Landesamt für Arbeitsschutz, Gesundheitsschutz und technische Sicherheit, Berlin, Germany). Informed written consent was obtained from each volunteer and patient prior to the study in compliance with the local institutional review board guidelines.

Sodium MRI was performed in seven healthy adult volunteers (3 female: mean age = 28.5 years, mean BMI = 22.0 kg/m²; 4 male: mean age = 33.5 years, mean BMI = 23.9 kg/m²). The volunteers were asked to put their heads inside the ¹H volume coil. Next the ²³Na 6-channel transceiver array was placed on the volunteers' cheeks, as shown in Figure 2c,f. The imaging session first involved proton imaging to provide an anatomical reference, employing a T₂-weighted 2D Rapid Acquisition with Relaxation Enhancement (RARE) technique (TR = 2940 ms; TE = 74 ms; spatial resolution = 0.54 x 0.54 mm²; FOV = 384 x 384 mm²; number of slices = 3; slice thickness = 1.4 mm; nominal refocusing FA = 120°, NA = 1. The acquisition time was 1 minute 8 seconds.

A 3D-DAPR imaging technique was used to perform sodium imaging of the eyes. The volunteers were asked to keep their eyes closed during the examination. No extra measures were applied to reduce eye motion. Both eyes were imaged at the same time. The nominal spatial resolutions were chosen based on the available SNR. The transceiver array that was placed in close

proximity to the eyes provides much higher SNR than traditional volume coils that are commonly used for ^{23}Na MRI of humans. Thus, the spatial resolution is closer to the resolutions achieved with sophisticated receive arrays at higher field strengths (36). This enables the delineation of various structures in the eye as well as potential pathologies. For instance, the mean axial and equator thickness of an average healthy human lens is about 4 mm (ranging from 3.5 mm to 4.5 mm) as well as 8.5 mm (ranging from 7.5 mm to 9.5 mm) respectively (43) and the mean anterior chamber depth, which is filled with aqueous humor, is around 3 mm ranging from 2 mm to 4 mm (44). Mean vitreous length is 16 mm ranging from, 14 mm to 18 mm (45). Typical intraocular masses of interest are between 1 mm and 3 mm in height and between 5 mm and 16 mm on the basis (46).

Pulse sequence parameters were chosen to achieve a compromise between short acquisition time, high spatial resolution and high SNR. The repetition time TR was varied between the two 1 mm isotropic spatial resolution scans to reduce the acquisition time by 3 min and 20 sec. To meet this goal the readout duration needed to be shortened accordingly. The images acquired with this setup provided lower SNR (due to shorter readout duration) than the data sets obtained with a scan time of 14 min 10 sec. Yet, all of the most important anatomical details were still prominent in the image acquired with the shorter scan time. We assumed T_1 to be similar to T_1 of CSF (47) ($T_1 \sim 65$ ms), which is a legitimate approach since CSF and vitreous humor showed reduced signal intensity in the corresponding ^{23}Na inversion recovery images. Although, T_1 -weighting was not our goal, we permitted T_1 weighting to achieve higher spatial resolution. We calculated the Ernst angle for the given T_1 : $FA_{\text{Ernst}} = 40^\circ$ for $TR = 17$ ms and $FA_{\text{Ernst}} = 35^\circ$ for $TR = 13$ ms. A nominal $FA = 41^\circ$ which is close the calculated Ernst flip angle was employed. TE was not constrained by the use of the proposed transceiver array. TE in the DAPR sequence is defined as the period of time between the middle of the rectangular excitation pulse and the beginning of the readout. The minimum time between the excitation pulse and the start of the readout is 50 μs . The latter is dictated by the transmit/receive switch hardware which governs the T/R switching time. T_2^* reported by Kohler et al. (30) for enucleated human eye was measured to be ~ 45 ms at 1.9 T. It is expected to be equal or shorter at 7 Tesla. Therefore, the parameters for 3D-DAPR imaging were chosen as follows:

a) For a nominal isotropic resolution of $1.4 \times 1.4 \times 1.4 \text{ mm}^3$: $TR = 13$ ms; $TE = 0.55$ ms; nominal $FA = 41^\circ$; number of projections = 50000; readout duration = 9.2 ms; radial samples = 520; maximum gradient amplitude = 18 mT/m; maximum gradient slew rate = 170 mT/m/s; pulse reference amplitude = 200 V. The acquisition time was 10 minutes 50 seconds.

b) For a nominal isotropic resolution of $1.0 \times 1.0 \times 1.0 \text{ mm}^3$: TR = 17 ms; TE = 0.55 ms; nominal FA = 41° ; number of projections = 50000; readout duration = 13.3 ms; radial samples = 864; maximum gradient amplitude = 22 mT/m; maximum gradient slew rate = 170 mT/m/s; pulse reference amplitude = 200 V. The acquisition time was 14 minutes 10 seconds.

c) For a nominal isotropic resolution of $1.0 \times 1.0 \times 1.0 \text{ mm}^3$: TR = 13 ms; TE = 0.55 ms; nominal FA = 41° ; number of projections = 50000; readout duration = 9.3 ms; radial samples = 864; maximum gradient amplitude = 25 mT/m; maximum gradient slew rate = 170 mT/m/s; pulse reference amplitude = 200 V. The acquisition time was 10 minutes 50 seconds.

Sodium images and B_1^+ maps were reconstructed offline in Matlab using custom made scripts. Full width at half maximum (FWHM) of the point spread function was simulated for a given range of T_{RO}/T_2^* . Even if we assume T_2^* much shorter than 45 ms, which is e.g. 30 ms, the FWHM value does not change substantially. It is fair to assume that for all of the sequence protocols, the FWHM is 2 pixels or less (including filtering).

Results

RF Coil Performance

The measured S-Matrix averaged over 9 volunteers (5 men and 4 women) is demonstrated in Figure 3. S_{11} values for all volunteers were found between -17.0 and -21.5 dB, S_{22} between -18.7 and -38.2 dB, S_{33} between -17.1 and -26.0 dB, S_{44} between -13.1 and -34.3 dB, S_{55} between -12.4 and -36.7 dB and S_{66} between -12.0 and -28.3 dB. Applying capacitive decoupling between elements 1 and 2 (and due to the symmetry of the circuit, between 4 and 5) and between 2 and 3 (or 5 and 6) yielded averaged transmission coefficient values of -16.4 dB for S_{12} (-14.0 dB for S_{45}) and -13.1 dB for S_{23} (-16.8 dB for S_{56}). Applying inductive decoupling between elements 1 and 3 (4 and 6) gave -17.8 dB for S_{13} (-17.7 dB for S_{46}) and between elements 3 and 6: -19.1 dB for S_{36} . The cylindrical phantom was used in order to evaluate the Q_{UL}/Q_L ratio for each loop element of the array. The measurements yielded the Q_{UL}/Q_L ratio as follows: element 1 – 1.8, element 2 – 2.1, element 3 – 1.3, element 4 – 1.7, element 5 – 1.6, element 6 – 1.3. The average Q factor value for all of the loops was estimated to be 1.6.

EMF and SAR simulations

The method used for B_1^+ optimization yielded more than one satisfying solution. We chose the one that provided the highest B_1^+ homogeneity within the extended mask, here called the phase-optimized setting (PO). The algorithm provided phases for PO as follows: channel 1: 0° , channel 2: -202° , channel 3: -186° , channel 4: -282° , channel 5: -246° , channel 6: -279° . The B_1^+ homogeneity for PO was assessed in the defined volume of interest (VOI) which covered both eyes of the human voxel models, yielding a standard deviation: SD = 15.8 % for Ella and SD = 15.2 % for Duke (Figure 4). Local SAR values averaged over 10 g (SAR_{10g}) were derived from the EMF simulations for PO using the human voxel models Duke and Ella (Figure 5) for an input power of 1 W. SAR simulations included the measured RF chain in order to accurately capture its losses and imperfections. Local SAR maxima were found to be 0.61 W/kg for Duke and 0.54 W/kg for Ella. Including a safety factor of 2.5, time-averaged forward power was limited to 6.7 W in order to stay below the 10 W/kg limit set by the IEC guidelines.

Phantom Experiments: B_1^+ Mapping

Phantom studies were conducted to compare the simulated B_1^+ distribution with the measured transmit field for PO which was later used for in vivo human imaging. A transversal slice through the center of the phantom was aligned with the center of the RF coil to determine whether there were differences between transmit field measurements and simulations (Figure 6a). The transmit field maps were in a very good agreement both qualitatively and quantitatively (Figure 6b). These results demonstrate validity of the RF coil design and support the credibility of the SAR simulations.

In vivo feasibility study

The in vivo feasibility study yielded high spatial resolution ^{23}Na MR images of the human eye at 7.0 T for female and male volunteers (Figure 7, 8 and 9). Another dataset obtained from a female subject is highlighted in Supporting Figure S1 in the supplemental material. Supporting Figure S2 in the supplemental material shows also an extra dataset obtained from a male subject. A nominal isotropic resolution of 1.4 mm^3 was achieved within an acquisition time (TA) of 10 minutes and 50 seconds. A nominal isotropic resolution of 1.0 mm^3 was achieved with TA = 14 minutes and 10 seconds. For the same spatial resolution, TA = 10 minutes and 50 seconds was used when TR was shortened to 13 ms. Three of the most important tissues in the context of sodium physiology can clearly be distinguished in all of the images: the vitreous humor, the aqueous humor and the lens. SNR estimation of the data was conducted for one eye (sagittal slice in Fig. 7, 8 and 9) for female and male volunteers. The vitreous humor showed a mean $\text{SNR}_{\text{male1}} \approx 17$, mean $\text{SNR}_{\text{male2}} \approx 21$ and mean $\text{SNR}_{\text{female}} \approx 28$ for the data with isotropic resolution of 1.4 mm^3 . A mean $\text{SNR}_{\text{male1}} \approx 7$, mean $\text{SNR}_{\text{male2}} \approx 8$ and mean $\text{SNR}_{\text{female}} \approx 12$ was observed for the data with isotropic resolution 1.0 mm^3 (TA = 10 min 50 sec). Aqueous humor yielded a mean $\text{SNR}_{\text{male1}} \approx 18$, mean $\text{SNR}_{\text{male2}} \approx 22$ and mean $\text{SNR}_{\text{female}} \approx 31$ for the acquisition using isotropic resolution of 1.4 mm^3 . A mean $\text{SNR}_{\text{male1}} \approx 7$, mean $\text{SNR}_{\text{male2}} \approx 8$ and mean $\text{SNR}_{\text{female}} \approx 13$ was obtained for the images acquired with an isotropic resolution of 1.0 mm^3 (TA = 10 min 50 sec). Signal-to-noise ratio averaged over all subjects involved in this study showed a mean $\text{SNR}_{\text{vitreous humor}} = 20 \pm 4$ and mean $\text{SNR}_{\text{aqueous humor}} = 21 \pm 5$ for the spatial resolution of 1.4 mm isotropic and mean $\text{SNR}_{\text{vitreous humor}} = 8 \pm 2$ and mean $\text{SNR}_{\text{aqueous humor}} = 9 \pm 2$ for the spatial resolution of 1.0 mm isotropic (TA = 10 min 50 sec). Images (central sagittal slice) obtained from female volunteers ($\text{SNR}_{\text{vitreous humor}} = 23 \pm 5$ and mean $\text{SNR}_{\text{aqueous humor}} = 25 \pm 6$) revealed higher SNR versus male

volunteers ($\text{SNR}_{\text{vitreous humor}} = 17 \pm 2$ and mean $\text{SNR}_{\text{aqueous humor}} = 18 \pm 2$). Following the literature no significant sex-dependent differences in sodium concentration in the eye are to be expected (48). The differences in SNR may arise from different coupling between the coil and the volunteer. It should be also noted that the RF coil geometry conforms slightly better to an average female head versus an average male head, which might induce the SNR difference found between male and female volunteers.

For data evaluation no sensitivity correction was applied. Data obtained for all of the receive channels were combined using the sum of squares method so that some of the lateral regions of the eyes can look brighter. ^{23}Na images of the brain including the eye, which were acquired for the same pulse sequence were reported by Nagel et al. (47). To confirm the enhancement in spatial resolution enabled by the proposed transceiver array, data were acquired for healthy volunteers using exactly the same pulse sequence parameters and imaging protocol as for the 1.4 mm spatial resolution scan with the exception that the spatial resolution was set to $3 \times 3 \times 3 \text{ mm}^3$. The latter mimics the “typical” spatial resolution accomplished with volume coils tailored for ^{23}Na MRI of the brain (47). For this purpose the gradient amplitude was reduced. Figure 9 surveys the data obtained with an isotropic spatial resolution of 3 mm, 1.4 mm and 1 mm and underscores the gain in spatial resolution performance enabled by the proposed transceiver array.

Discussion and Conclusions

This work demonstrates that the proposed six-channel transceiver array supports high-spatial resolution, in vivo sodium imaging of the human eye at 7.0 T. We obtained images with a nominal isotropic resolution of 1.4 mm^3 and 1.0 mm^3 , both achieved within a clinically acceptable scan time of about 10 minutes. The quality of the images permits clear distinctions between the vitreous humor, the aqueous humor and the lens. The RF coil is light-weight and can be applied to an average human head. To maintain patient comfort an extra mask made of very soft material was placed between the RF coil and the volunteer's face. This solution provides comfort and eliminates the problem of mismatch between the edges of the casing and the shape of volunteer's face. This approach preserves the coil's light weight (around 600 g). Possible movement of the coil was eliminated by adding sponges between the transceiver array and the volume coil.

Our measurements reveal an acceptable level of sensitivity to different loading conditions that should not be an issue when being used with patients. B_1^+ optimization yielded a phase setting with ample B_1^+ homogeneity within both eyes and low SAR values for both human voxel models Duke and Ella. Measured and simulated transmit field maps showed very good agreement. The proposed RF coil fulfills the safety requirements for local transmit arrays and presents no obstacles to future patient studies. The DAPR method is less susceptible to artifacts caused by B_0 -inhomogeneities compared to conventional radial sampling (42). We do not expect visible distortion or signal dropouts due to B_0 -inhomogeneities with the applied parameters. However, we did not correct for the B_1 profile of the coil which results in slight inhomogeneities.

Our design departs in several respects from others found in the literature. To our knowledge, it is the first study which uses a dedicated RF coil to carry out ^{23}Na imaging of the human eye in vivo. As stated earlier, the only prior attempts to image sodium in the eye in vivo have focused on sodium imaging of the brain. These investigations were done at lower field strengths than ours, using sub-optimal RF set-ups in the context of eye imaging. For instance, Shen et al. (33) used dual-tuned birdcage at 1.5 T. Lommen et al. (49) and Madelin and Regatte (34) performed an experiment at 3.0 T with a volume coil as well. Qian et al. (24) carried out sodium imaging of the brain at 7.0 T with a birdcage coil and 15-channel receive-only array. It is hard to use that study as a reference because signal from the eyes was cut away in the image. Shajan et al. (36) proposed a ^{23}Na 4-channel transceiver and ^{23}Na 27-channel receive-only array; used together, they supported sodium imaging of the brain at 9.4 T, a field strength higher

than reported here. Their results could be considered as comparable with ours. However, the receive-only coil they used was optimized for whole brain imaging, with much larger array loops. It introduces additional noise in the context of eye imaging and can be further optimized.

One issue relevant to this design that does not affect the validity of the findings should be noted as an area for further improvement. We used inductive decoupling to reduce severe coupling between non-adjacent elements, but this method is a costly solution. The issue affects both the efficiency of transmission and SNR and becomes apparent when the Q_{UL}/Q_L ratio is analyzed for all the elements. As expected, the ratios are lowest for elements 3 and 6, which are overloaded with inductors. At lower frequencies, RF coils do not couple as strongly to the load – a reason we expected the Q_{UL}/Q_L ratio to be worse than that found, for example, at 300 MHz (the resonant frequency of protons at 7.0 T), however these losses should be considered as new designs are developed. One obvious solution would be to use a multi-channel receive-only array, which would probably provide benefits in terms of SNR, but this would require the design of a transmit-only (or transceiver) volume or semi-volume coil. This could be accomplished with either dual-tuned ($^{23}\text{Na}/^1\text{H}$) coil or two separate coils. For example, an ^{23}Na transmit array and a nested configuration for ^1H could be applied.

The potential of this project for clinical applications derives from the role of sodium in eye physiology. This discussion will consider the vitreous humor (VH), aqueous humor (AH) and the lens – tissues which are particularly clear in our images – as well as the retina, due to its key role in processing optical signals.

The concentration of Na^+ in the vitreous should be close to that of plasma, at around 135 mmol/l (11). Changes in concentrations of substances in the vitreous body likely reflect processes in adjoining tissues.

Active secretion accounts for 80-90% of total AH formation and is driven by primary active transport of sodium ions (11). This triggers the movement of other molecules through cell membranes. The functions of other co-transporters such as Na^+/H^+ and Na-K-2Cl, which are involved in further processes, require sodium ions as well. This emphasizes the importance that Na^+ plays in AH formation and potential reabsorption.

Sodium ions are also essential for the normal functioning of the retina (11). The elimination of an excessive amount of water is driven by Na^+/K^+ -ATPase located in the retinal pigment epithelium (RPE). Lactic acid is removed by the monocarboxylate transporter, which is driven by the activity of Na^+/H^+ exchanger.

The sodium concentration in the lens is much lower than in the VH, reported to be around 20 mmol/l (15). Ion circulation between the lens and the VH provides nutrients for the lens. This

concentration gradient is driven by the activity of Na^+/K^+ -ATPase, located in the lens epithelium (50).

The crucial roles of these processes involving sodium ions, as well as their roles in tissue homeostasis, suggest that various pathologies may lead to abnormal sodium concentrations in the fluid compartments and tissues of the eye. Since these changes could be detectable in MRI, it is quite plausible that a non-invasive method of measuring sodium concentrations in patients with various eye disorders will contribute to our understanding of disease pathologies and also yield diagnostic information. A consideration of what is known about glaucoma and cataracts, which are the leading causes of blindness, and eye tumors, can provide an indication of the role of sodium and the potential changes it undergoes during the development of these diseases.

The lack of tissue sodium concentration quantification is a recognized limitation of this feasibility study. We are acutely aware that an accurate quantification of sodium content of the eye's compartments requires a very well-validated algorithm. This could include placing external ^{23}Na concentration standards into the target region. Instead we propose to build a phantom with proper T_1 and T_2 relaxation characteristics, which couples to the RF coil almost like a human head. Tissue sodium content quantification also requires B_0 field, transmit field and sensitivity correction. Another issue that needs to be addressed *en route* to reliable tissue sodium quantification is the correction of eye movements. This correction is of most relevance for smaller compartments such as the aqueous humor and the lens. Therefore we anticipate the implementation of an eye tracking system. Sodium in vivo imaging of the human eye in patients has not been reported yet. Our knowledge is based on ex vivo studies. Therefore we cannot be absolutely sure what kind and magnitude of signal intensity or sodium concentration changes are to be expected for diseases and disorders of the eye under in vivo conditions. We suggest to break ground *via* a qualitative identification of these changes first in a small patient cohort as a mandatory precursor to broader patient studies involving tissue sodium content quantification.

The biomedical literature contains multiple reports of elevated sodium content in tumors (19,20,51). Sodium imaging of the human eye in vivo at 7.0 T could be used as a complement to proton imaging data that might help in the planning of radiation treatments for which the UHF-MRI safety of ocular tantalum markers has been recently demonstrated (52). Another potential use would be as a follow-up to proton beam therapy of intraocular tumors.

Glaucoma is often associated with higher intraocular pressure (IOP). Ascher (17) reported diminished sodium levels in AH of glaucomatous eyes. Cole (53) found that reducing plasma sodium concentration and thereby plasma osmolarity, led to a decrease in concentrations of sodium in the AH and an increase in IOP which lasted for several hours. The

notion is further supported by the finding that hyponatremia probably contributes to the pathophysiology of bilateral acute angle closure glaucoma (18).

The characteristics of cataracts also suggest that sodium levels might be informative. The Na^+/K^+ gradient between the lens and vitreous humor is maintained by Na^+/K^+ -ATPase in the epithelial cell layer of the lens. Ex vivo studies have repeatedly reported elevated sodium concentrations in cataractous lenses (15,16).

The ultimate goal of this work is to provide a method which will allow assessment of TSC in the eye and its compartments in vivo, within time frames suitable for clinical applications. Our results support the statement that sodium content in the lens is distinguishable from sodium content in the aqueous and vitreous humor. The pathologic alterations discussed above reveal that these observations might have clinical importance in a number of contexts. The broad roles of this element in processes related to eye physiology suggest a range of questions for ophthalmological investigations.

Acknowledgements

The authors wish to acknowledge Darius Lysiak (MRI.TOOLS GmbH, Berlin, Germany) for his help with practical aspects of the RF coil design; Aaron Kujawa and Kristian Rink (German Cancer Research Center (DKFZ), Heidelberg, Germany) for providing the phase-sensitive method for transmit field mapping; Oliver Stangl (Max-Delbrück Center for Molecular Medicine in the Helmholtz Association, Berlin, Germany) for his help at the initial stage of the project and Lukas Winter (Max-Delbrück Center for Molecular Medicine in the Helmholtz Association, Berlin, Germany) for helpful discussions. This work was funded (in part, T.N.) by the Helmholtz Alliance ICEMED - Imaging and Curing Environmental Metabolic Diseases, through the Initiative and Network Fund of the Helmholtz Association (ICEMED-Project 1210251).

References

1. Richdale K, Wassenaar P, Teal Bluestein K, Abduljalil A, Christoforidis JA, Lanz T, Knopp MV, Schmalbrock P. 7 Tesla MR imaging of the human eye in vivo. *J Magn Reson Imaging*. 2009;30:924-932.
2. Graessl A, Muhle M, Schwerter M, et al. Ophthalmic magnetic resonance imaging at 7 T using a 6-channel transceiver radiofrequency coil array in healthy subjects and patients with intraocular masses. *Invest Radiol*. 2014;49:260-270.
3. Lindner T, Langner S, Graessl A, et al. High spatial resolution in vivo magnetic resonance imaging of the human eye, orbit, nervus opticus and optic nerve sheath at 7.0 Tesla. *Exp Eye Res*. 2014;125:89-94.
4. Singh AD, Platt SM, Lystad L, Lowe M, Oh S, Jones SE, Alzahrani Y, Plesec T. Optic Nerve Assessment Using 7-Tesla Magnetic Resonance Imaging. *Ocul Oncol Pathol*. 2016;2:178-180.
5. Christoforidis JB, Wassenaar PA, Christoforidis GA, Ho VY, Knopp MV, Schmalbrock PM. Retrobulbar vasculature using 7-T magnetic resonance imaging with dedicated eye surface coil. *Graefes Arch Clin Exp Ophthalmol*. 2013;251:271-277.
6. Beenakker JW, van Rijn GA, Luyten GP, Webb AG. High-resolution MRI of uveal melanoma using a microcoil phased array at 7 T. *NMR Biomed*. 2013;26:1864-1869.
7. Walter U, Niendorf T, Graessl A, Rieger J, Kruger PC, Langner S, Guthoff RF, Stachs O. Ultrahigh field magnetic resonance and colour Doppler real-time fusion imaging of the orbit--a hybrid tool for assessment of choroidal melanoma. *Eur Radiol*. 2014;24:1112-1117.

8. Lindner T, Langner S, Falke K, et al. Anatomic and pathological characterization of choroidal melanoma using multimodal imaging: what is practical, what is needed? *Melanoma Res.* 2015;25:252-258.
9. Beenakker JW, Ferreira TA, Soemarwoto KP, Genders SW, Teeuwisse WM, Webb AG, Luyten GP. Clinical evaluation of ultra-high-field MRI for three-dimensional visualisation of tumour size in uveal melanoma patients, with direct relevance to treatment planning. *MAGMA.* 2016;29:571-577.
10. Paul K, Graessl A, Rieger J, et al. Diffusion-sensitized ophthalmic magnetic resonance imaging free of geometric distortion at 3.0 and 7.0 T: a feasibility study in healthy subjects and patients with intraocular masses. *Invest Radiol.* 2015;50:309-321.
11. Kaufman PL, Adler FH, Levin LA, Alm A. *Adler's Physiology of the Eye.* Elsevier Health Sciences 2011.
12. Bonanno JA. Molecular mechanisms underlying the corneal endothelial pump. *Exp Eye Res.* 2012;95:2-7.
13. Eye Diseases Statistics. <https://www.nei.nih.gov/eyedata/cataract>: National Eye Institute; 2014.
14. Eye Diseases Statistics. <https://www.nei.nih.gov/eyedata/glaucoma>: National Eye Institute; 2014.
15. Garner WH, Hilal SK, Lee SW, Spector A. Sodium-23 magnetic resonance imaging of the eye and lens. *Proc Natl Acad Sci U S A.* 1986;83:1901-1905.

16. Chandorkar AG, Albal MV, Bulakh PM, Gumaste VV. Electrolyte pattern in normal goat lenses and its alteration in lens culture during cataractogenesis. *Indian J Ophthalmol.* 1983;31:262-264.
17. Ascher KW. Zur Chemie des menschlichen Kammerwassers. *Graefe's Archive for Clinical and Experimental Ophthalmology.* 1922;107:247-297.
18. Chen SH, Karanjia R, Chevrier RL, Marshall DH. Bilateral acute angle closure glaucoma associated with hydrochlorothiazide-induced hyponatraemia. *BMJ Case Rep.* 2014;2014.
19. Ouwerkerk R, Bleich KB, Gillen JS, Pomper MG, Bottomley PA. Tissue sodium concentration in human brain tumors as measured with ²³Na MR imaging. *Radiology.* 2003;227:529-537.
20. Ouwerkerk R, Jacobs MA, Macura KJ, Wolff AC, Stearns V, Mezban SD, Khouri NF, Bluemke DA, Bottomley PA. Elevated tissue sodium concentration in malignant breast lesions detected with non-invasive ²³Na MRI. *Breast Cancer Res Treat.* 2007;106:151-160.
21. Siegel RL, Miller KD, Jemal A. Cancer statistics, 2016. *CA: a cancer journal for clinicians.* 2016;66:7-30.
22. Haneder S, Michaely HJ, Schoenberg SO, Konstandin S, Schad LR, Siebenlist K, Wertz H, Wenz F, Lohr F, Boda-Heggemann J. Assessment of renal function after conformal radiotherapy and intensity-modulated radiotherapy by functional ¹H-MRI and ²³Na-MRI. *Strahlenther Onkol.* 2012;188:1146-1154.
23. Wetterling F, Corteville DM, Kalayciyan R, Rennings A, Konstandin S, Nagel AM, Stark H, Schad LR. Whole body sodium MRI at 3T using an asymmetric birdcage resonator and short echo time sequence: first images of a male volunteer. *Phys Med Biol.* 2012;57:4555-4567.

24. Qian Y, Zhao T, Wiggins GC, Wald LL, Zheng H, Weimer J, Boada FE. Sodium imaging of human brain at 7 T with 15-channel array coil. *Magn Reson Med*. 2012;68:1807-1814.
25. Haneder S, Juras V, Michaely HJ, Deligianni X, Bieri O, Schoenberg SO, Trattnig S, Zbyn S. In vivo sodium (^{23}Na) imaging of the human kidneys at 7 T: preliminary results. *Eur Radiol*. 2014;24:494-501.
26. Resetar A, Hoffmann SH, Graessl A, Winter L, Waiczies H, Ladd ME, Niendorf T, Nagel AM. Retrospectively-gated CINE (^{23}Na) imaging of the heart at 7.0 Tesla using density-adapted 3D projection reconstruction. *Magn Reson Imaging*. 2015;33:1091-1097.
27. Graessl A, Ruehle A, Waiczies H, Resetar A, Hoffmann SH, Rieger J, Wetterling F, Winter L, Nagel AM, Niendorf T. Sodium MRI of the human heart at 7.0 T: preliminary results. *NMR Biomed*. 2015;28:967-975.
28. Linz P, Santoro D, Renz W, et al. Skin sodium measured with (^{23}Na) MRI at 7.0 T. *NMR Biomed*. 2015;28:54-62.
29. Kolodny NH, Gragoudas ES, D'Amico DJ, Kohler SJ, Seddon JM, Murphy EJ, Yun C, Albert DM. Proton and sodium 23 magnetic resonance imaging of human ocular tissues. A model study. *Arch Ophthalmol*. 1987;105:1532-1536.
30. Kohler SJ, Kolodny NH, D'Amico DJ, Balasubramaniam S, Mainardi P, Gragoudas ES. Magnetic resonance imaging determination of ^{23}Na visibility and $T2^*$ in the vitreous body. *Journal of Magnetic Resonance (1969)*. 1989;82:505-517.
31. Kohler SJ, Kolodny NH, Celi AC, Burr TA, Weinberg D, D'Amico DJ, Gragoudas ES. In vivo sodium chemical shift imaging. *Magn Reson Med*. 1992;23:77-88.

32. Kolodny NH, Kohler SJ, Rettig ES, Botti PA, D'Amico DJ, Gragoudas ES. A feasibility study of ²³Na magnetic resonance imaging of human and rabbit vitreal disorders. *Invest Ophthalmol Vis Sci.* 1993;34:1917-1922.
33. Shen GX, Boada FE, Thulborn KR. Dual-frequency, dual-quadrature, birdcage RF coil design with identical B1 pattern for sodium and proton imaging of the human brain at 1.5 T. *Magn Reson Med.* 1997;38:717-725.
34. Madelin G, Regatte RR. Biomedical applications of sodium MRI in vivo. *J Magn Reson Imaging.* 2013;38:511-529.
35. Stobbe R, Beaulieu C. In vivo sodium magnetic resonance imaging of the human brain using soft inversion recovery fluid attenuation. *Magn Reson Med.* 2005;54:1305-1310.
36. Shajan G, Mirkes C, Buckenmaier K, Hoffmann J, Pohmann R, Scheffler K. Three-layered radio frequency coil arrangement for sodium MRI of the human brain at 9.4 Tesla. *Magn Reson Med.* 2016;75:906-916.
37. Kumar A, Edelstein WA, Bottomley PA. Noise figure limits for circular loop MR coils. *Magn Reson Med.* 2009;61:1201-1209.
38. Christ A, Kainz W, Hahn EG, et al. The Virtual Family--development of surface-based anatomical models of two adults and two children for dosimetric simulations. *Phys Med Biol.* 2010;55:N23-38.
39. Kuehne A, Goluch S, Waxmann P, Seifert F, Ittermann B, Moser E, Laistler E. Power balance and loss mechanism analysis in RF transmit coil arrays. *Magn Reson Med.* 2015;74:1165-1176.
40. Deb K. Multi-objective optimization using evolutionary algorithms. Wiley 2005.

41. Morrell GR. A phase-sensitive method of flip angle mapping. *Magn Reson Med.* 2008;60:889-894.
42. Nagel AM, Laun FB, Weber MA, Matthies C, Semmler W, Schad LR. Sodium MRI using a density-adapted 3D radial acquisition technique. *Magn Reson Med.* 2009;62:1565-1573.
43. Schachar RA. Growth patterns of fresh human crystalline lenses measured by in vitro photographic biometry. *J Anat.* 2005;206:575-580.
44. Zamir E, Kong GY, Kowalski T, Coote M, Ang GS. A Novel Method of Quantitative Anterior Chamber Depth Estimation Using Temporal Perpendicular Digital Photography. *Transl Vis Sci Technol.* 2016;5:10.
45. Roters S, Hellmich M, Szurman P. Prediction of axial length on the basis of vitreous body length and lens thickness: retrospective echobiometric study. *J Cataract Refract Surg.* 2002;28:853-859.
46. Guthoff RF, Labriola LT, Stachs O. Diagnostic ophthalmic ultrasound. In: *Retina Fifth Edition: Elsevier Inc.;* 2012.
47. Nagel AM, Bock M, Hartmann C, et al. The potential of relaxation-weighted sodium magnetic resonance imaging as demonstrated on brain tumors. *Invest Radiol.* 2011;46:539-547.
48. Kokavec J, Min SH, Tan MH, Gilhotra JS, Newland HS, Durkin SR, Grigg J, Casson RJ. Biochemical analysis of the living human vitreous. *Clin Exp Ophthalmol.* 2016;44:597-609.
49. Lommen J, Konstandin S, Kramer P, Schad LR. Enhancing the quantification of tissue sodium content by MRI: time-efficient sodium B1 mapping at clinical field strengths. *NMR Biomed.* 2016;29:129-136.

50. Reddy VN. Transport of organic molecules in the lens. *Exp Eye Res.* 1973;15:731-750.

51. Cameron IL, Smith NK, Pool TB, Sparks RL. Intracellular concentration of sodium and other elements as related to mitogenesis and oncogenesis in vivo. *Cancer Res.* 1980;40:1493-1500.

52. Oberacker E, Paul K, Huelnhagen T, et al. Magnetic resonance safety and compatibility of tantalum markers used in proton beam therapy for intraocular tumors: A 7.0 Tesla study. *Magn Reson Med.* 2016.

53. Cole DF. Some effects of decreased plasma sodium concentration on the composition and tension of the aqueous humour. *Br J Ophthalmol.* 1959;43:268-287.

Figure captions:

Figure 1: Left: A view obtained from the CST Studio 2015 illustrating the head of the human voxel model Duke together with the proposed 6-channel transceiver RF array. Red arrows represent discrete ports used for the EMF simulations. Right: The schematic of the 6-channel transceiver RF array. Every channel was tuned to the resonant frequency with a tuning capacitor (C_{Ti} , $i=\{1,\dots,6\}$) and matched to the $50\ \Omega$ impedance with a matching capacitor (C_{Mi} , $i=\{1,\dots,6\}$). Trimmer capacitors were used to decouple element 1 and element 2 (C_{D12}) as well as elements 2 and 3 (C_{D23}). Due to the symmetry of the circuit, the same method was applied to decouple elements 4 and 5 and elements 5 and 6. Inductors used for decoupling of channels: 1 and 3, 4 and 6, and 3 and 6, are denoted as: L_{D13} , L_{D46} and L_{D36} . Inductors L_{D13} and L_{D46} were built as two-turn solenoids and inductors L_{D36} were built as a one-turn solenoid (wire thickness = 1 mm, inner diameter = 6 mm). Their inductances were slightly modified during the process of tuning and matching in order to reduce coupling to an acceptable level.

Figure 2: (A) The final version of the circuit illustrated in Fig. 1: copper loops soldered together with capacitors, inductors, cables and cable traps (wrapped with blue rubber). The whole structure is placed on the casing's bottom part and shown with the upper part of the casing next to it. (B) ^{23}Na six channel transceiver RF array placed on the cylindrical phantom. This set-up was used for the validation of the transmit field simulations. (C) The array placed on the face of an adult volunteer. (D) Six-way power divider using Wilkinson approach. (E) Multipurpose interface box which supports $^{23}\text{Na}/^1\text{H}$ imaging at 7.0 Tesla. (F) $^{23}\text{Na}/^1\text{H}$ imaging set-up: a volunteer together with the ^{23}Na six channel transceiver RF array inside the ^1H volume coil.

Figure 3: S-Parameter matrix averaged over 9 volunteers. Averaged values for reflection coefficients were found to be: -19.8 dB for S_{11} , -24.2 dB for S_{22} , -22.5 dB for S_{33} , -21.5 dB for S_{44} , -25.0 dB for S_{55} , -20.1 dB for S_{66} . The highest coupling occurs between elements 2/6 and between loop-elements which were capacitively decoupled: 2/3 and 4/5.

Figure 4: Transmit field (B_1^+) distribution for the phase-optimized setting (PO, channel 1: 0° , channel 2: -202° , channel 3: -186° , channel 4: -282° , channel 5: -246° , channel 6: -279°) in the sagittal, the coronal and the axial plane for human voxel models: Ella (top row) and Duke (bottom row). The red contours represent region of interest (ROI) covering the left and right eye

which was used for estimation of B_1^+ homogeneity. It contains all tissues which are considered in the voxel model to belong to the eye: the vitreous humor, the sclera, the cornea and the lens. The black contours represent the extended mask which was provided an error margin and was used for the transmit field optimization.

Figure 5: SAR_{10g} distribution for human voxel models Duke (left) and Ella (right) shown in 3D (top row) and for an axial view through the center of the eyes (bottom row). SAR_{10g} distributions were scaled to the maximum SAR_{10g} value for Duke (0.61 W/kg) in order to highlight good qualitative and quantitative (0.54 W/kg maximum SAR_{10g} value for Ella) agreement between SAR distributions for both human voxel models. The RF chain (its S-Matrix was measured by using a network analyzer) was included in the SAR simulations. Differences in SAR values arise from the anatomical differences between both models (mainly due to variations in shape of the skull and the nose).

Figure 6: (A) Simulated (left) and measured (right) B_1^+ field distribution in a central axial slice of the cylindrical phantom. B_1^+ field was measured by using a phase-sensitive method. Two images with nominal flip angle $FA = 90^\circ$ were acquired: one with the non-selective composite pulse [$2\alpha_0 \alpha_{90}$] and the other one with the first sub-pulse reversed in sign [$2\alpha_{180} \alpha_{90}$]. Pulse duration was 500 μ s. The following parameters were used: TR= 160 ms, TE = 0.5 ms, number of projections = 15000, radial samples = 732, max gradient amplitude = 4 mT/m, max gradient slew rate = 170 mT/m/s, nominal isotropic resolution = 3.0 x 3.0 x 3.0 mm³, pulse reference amplitude = 75 V. Flip angle maps were normalized to the RF input power. Four different profiles (I, II, III and IV) were drawn in both pictures. Light green color represents profiles for the simulated B_1^+ map and red color represents profiles for the measured B_1^+ map. (B) Quantitative comparison between all simulated and measured profiles. Simulated and measured data show very good agreement.

Figure 7: In vivo ²³Na image of the eyes of a healthy male volunteer (age = 26 years; BMI = 27.1 kg/m²) obtained with DA-3DPR imaging and filtered with Hamming filter demonstrated in sagittal and axial view. No method for sensitivity correction was applied. First row: nominal isotropic resolution = 1.4 x 1.4 x 1.4 mm³ was achieved within 10 minutes 50 seconds by using following parameters: TR/TE = 13/0.55 ms, number of projections = 50000, readout duration = 9.2 ms. Second row: nominal isotropic resolution = 1.0 x 1.0 x 1.0 mm³ was achieved within 14 minutes 10 seconds by using following parameters: TR/TE = 17/0.55 ms, number of projections = 50000, readout duration = 13.3 ms. Third row: nominal isotropic resolution = 1.0 x 1.0 x 1.0 mm³ was achieved within 10 minutes 50 seconds by using following parameters: TR/TE =

13/0.55 ms, number of projections = 50000, readout duration = 9.3 ms. Bottom row: proton reference images obtained with ^1H basic coil (Siemens, Erlangen, Germany) and T_2 -weighted RARE imaging: TR/TE = 2940/74 ms, FOV = 384 x 384 mm², in-plane resolution = 0.54 x 0.54 mm², FA = 120°.

Figure 8: In vivo ^{23}Na image of the eyes of a healthy female volunteer (age = 29 years; BMI = 19.2 kg/m²) obtained using the same pulse sequence parameters, imaging protocol and procedure as for the male volunteer shown in Figure 7.

Figure 9: In vivo ^{23}Na image of the eyes of a healthy male volunteer (age = 53 years; BMI = 23.5 kg/m²) obtained with an isotropic spatial resolution of 3 mm (top), 1.4 mm (middle) and 1.0 mm (bottom). A comparison between the low resolution data (3 mm isotropic) and the high resolution data (1.4 and 1.0 mm isotropic) facilitated by the performance gain of the proposed transceiver array underscores the need for enhanced spatial resolution to delineate all of the most important eye compartments.

Supporting Figure S1: In vivo ^{23}Na image of the eyes of a healthy female volunteer (age = 29 years; BMI = 21.8 kg/m²) obtained with DA-3DPR imaging and filtered with Hamming filter demonstrated in sagittal and axial view. No method for sensitivity correction was applied. First row: nominal isotropic resolution = 1.4 x 1.4 x 1.4 mm³ was achieved within 10 minutes 50 seconds by using following parameters: TR/TE = 13/0.55 ms, number of projections = 50000, readout duration = 9.2 ms. Second row: nominal isotropic resolution = 1.0 x 1.0 x 1.0 mm³ was achieved within 14 minutes 10 seconds by using following parameters: TR/TE = 17/0.55 ms, number of projections = 50000, readout duration = 13.3 ms. Third row: nominal isotropic resolution = 1.0 x 1.0 x 1.0 mm³ was achieved within 10 minutes 50 seconds by using following parameters: TR/TE = 13/0.55 ms, number of projections = 50000, readout duration = 9.3 ms. Bottom row: proton reference images obtained with ^1H basic coil (Siemens, Erlangen, Germany) and T_2 -weighted RARE imaging: TR/TE = 2940/74 ms, FOV = 384 x 384 mm², in-plane resolution = 0.54 x 0.54 mm², FA = 120°.

Supporting Figure S2: In vivo ^{23}Na image of the eyes of a healthy male volunteer (age = 30 years; BMI = 25.3 kg/m²) obtained using the same pulse sequence parameters, imaging protocol and procedure as for the female volunteer shown in Supporting Figure S1.

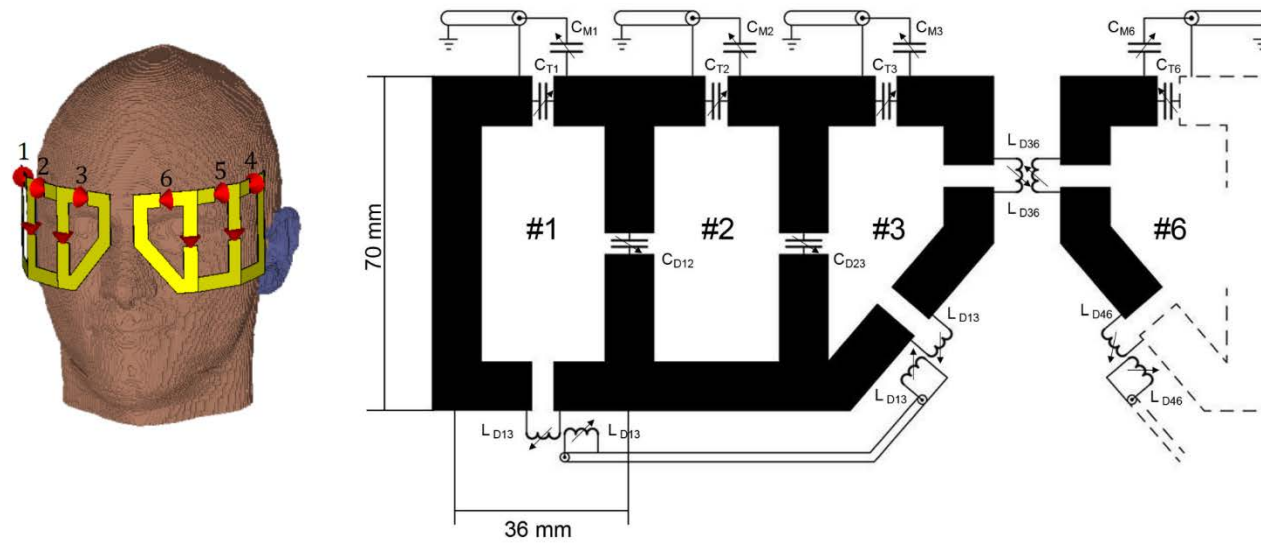


Figure 1

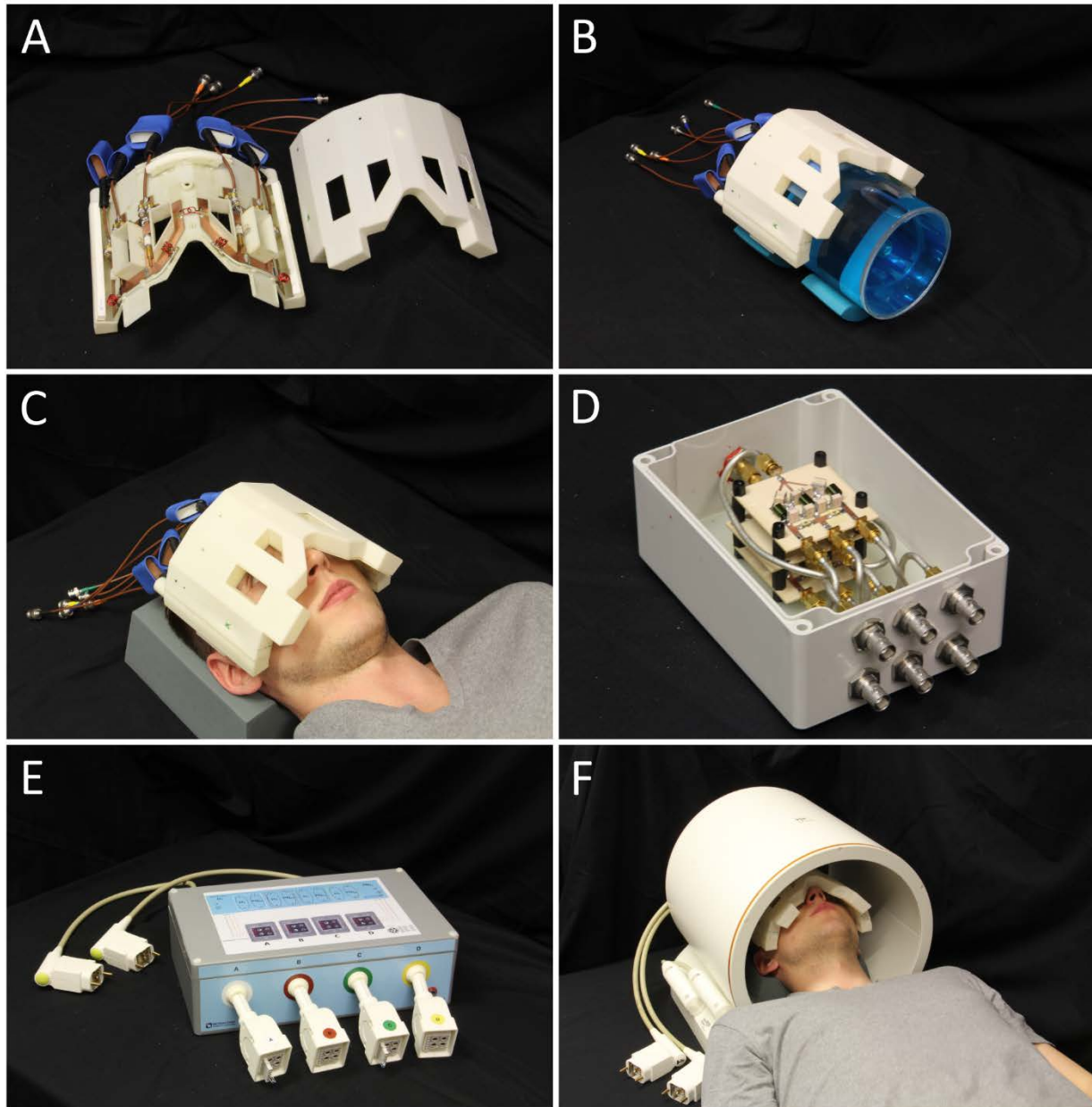


Figure 2

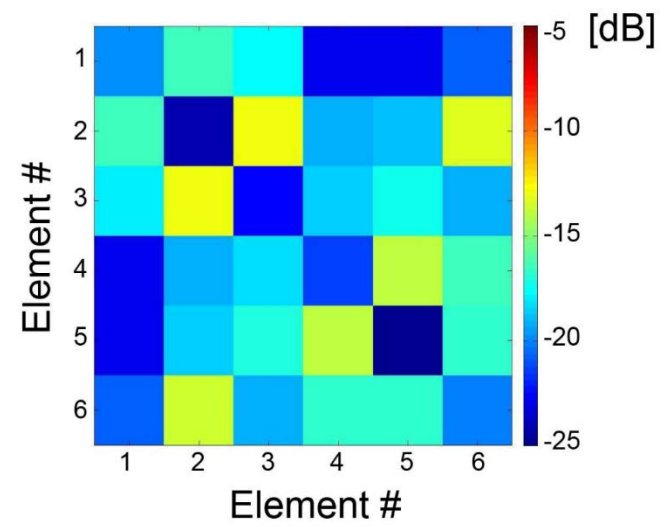


Figure 3

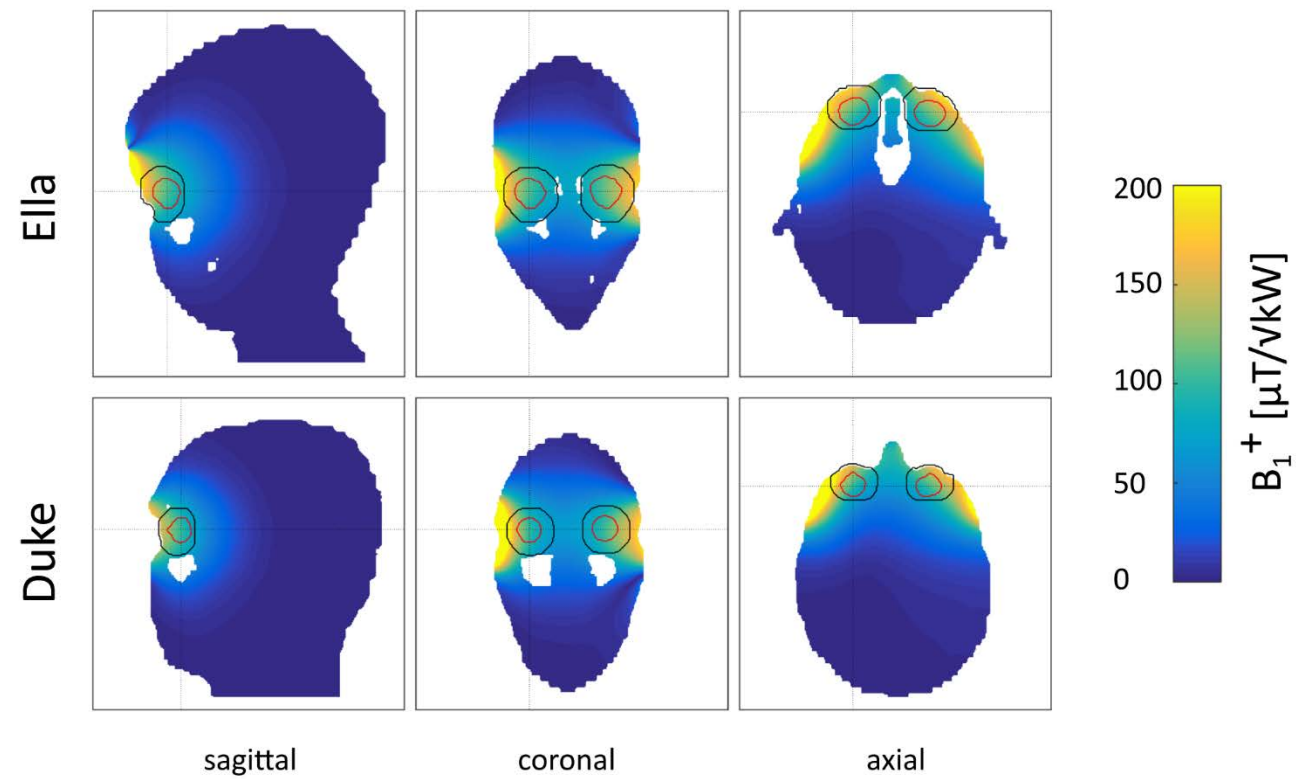


Figure 4

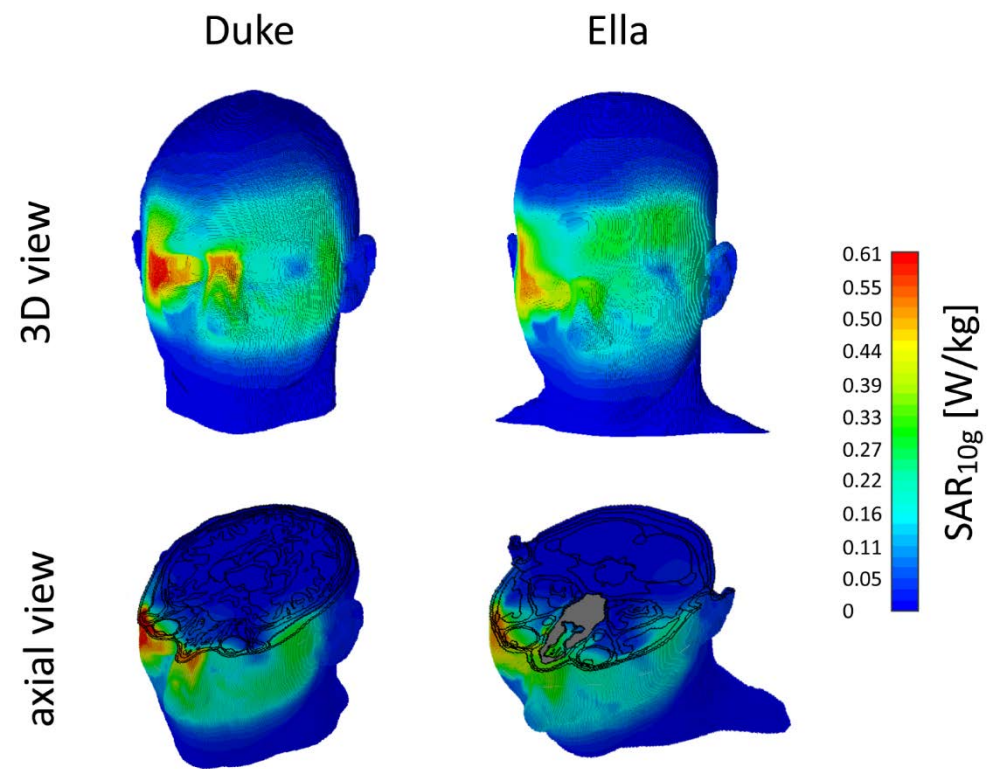


Figure 5

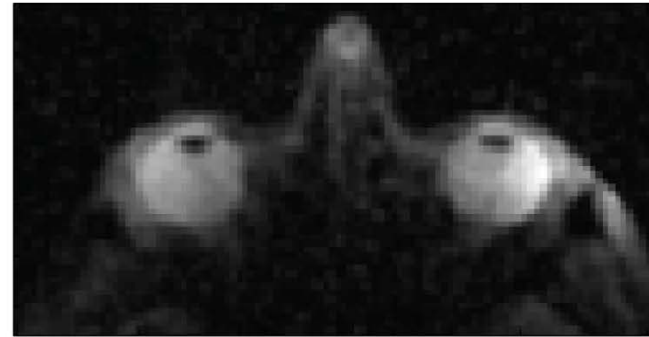
Figure 7

sagittal

axial

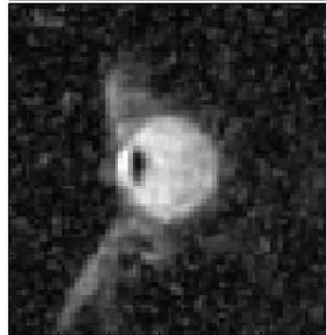
^{23}Na image
(1.4 x 1.4 x 1.4)
 mm^3

10 min 50 s



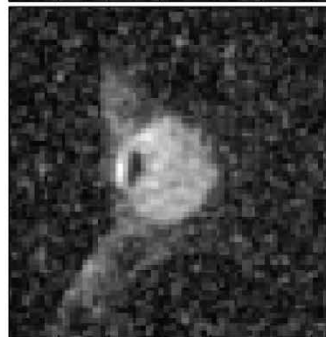
^{23}Na image
(1.0 x 1.0 x 1.0)
 mm^3

14 min 10 s



^{23}Na image
(1.0 x 1.0 x 1.0)
 mm^3

10 min 50 s



^1H image



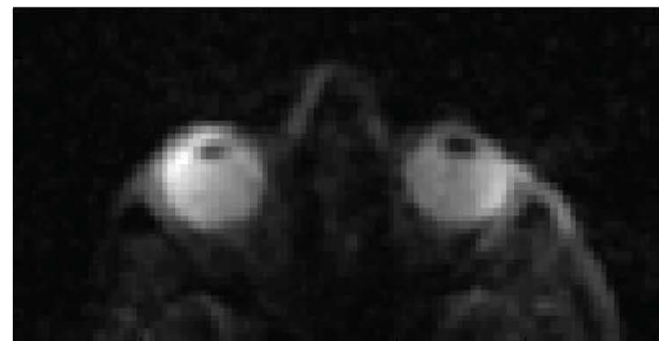
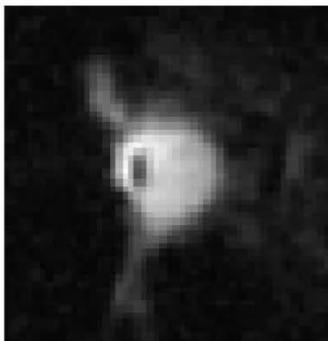
Figure 8

sagittal

axial

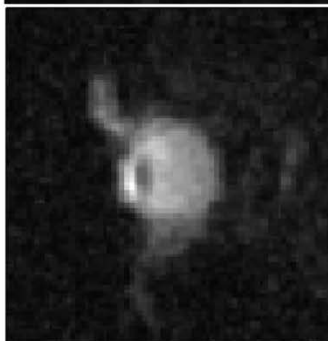
^{23}Na image
(1.4 x 1.4 x 1.4)
 mm^3

10 min 50 s



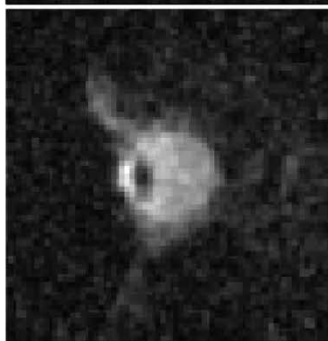
^{23}Na image
(1.0 x 1.0 x 1.0)
 mm^3

14 min 10 s



^{23}Na image
(1.0 x 1.0 x 1.0)
 mm^3

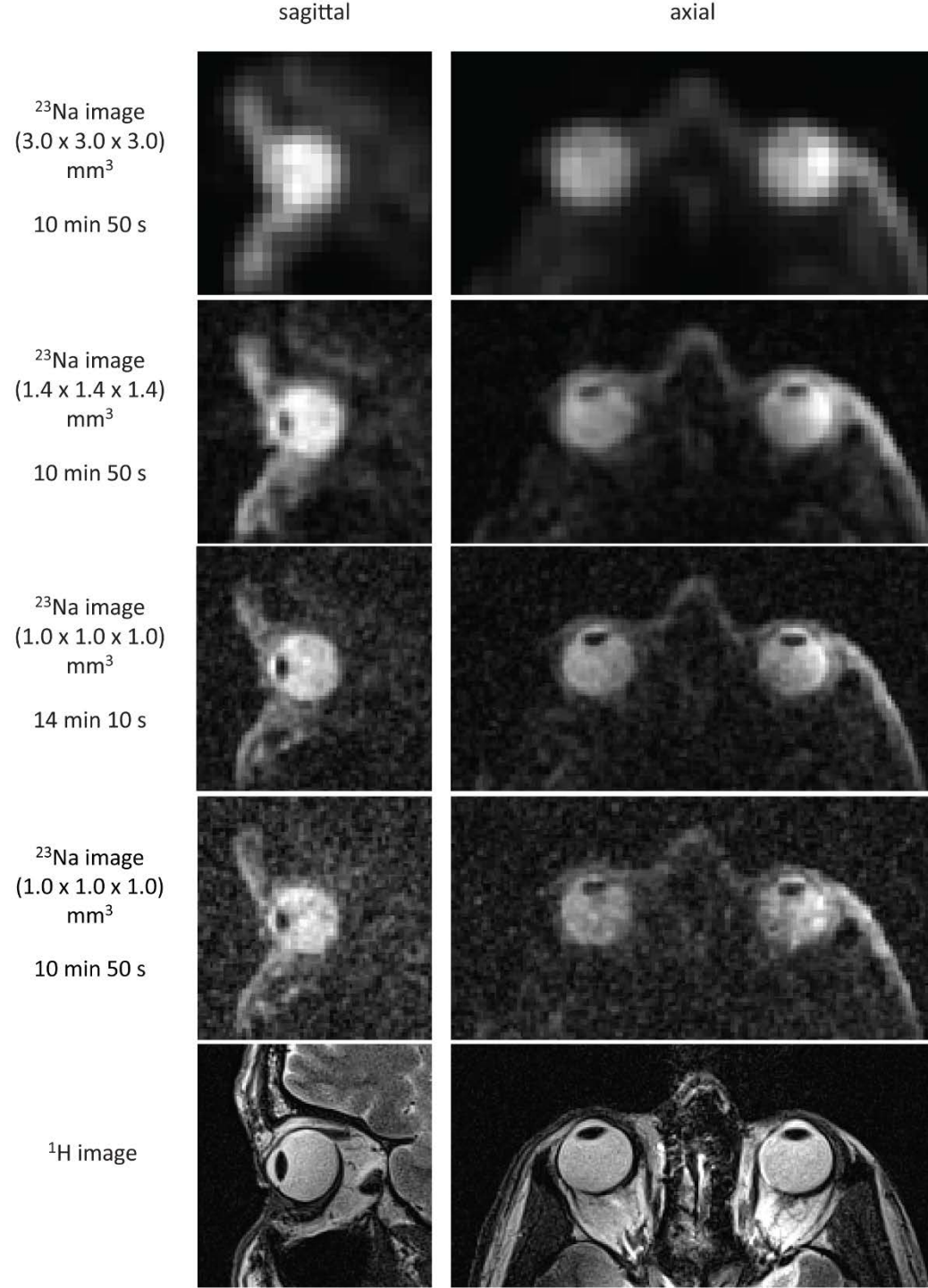
10 min 50 s



^1H image



Figure 9



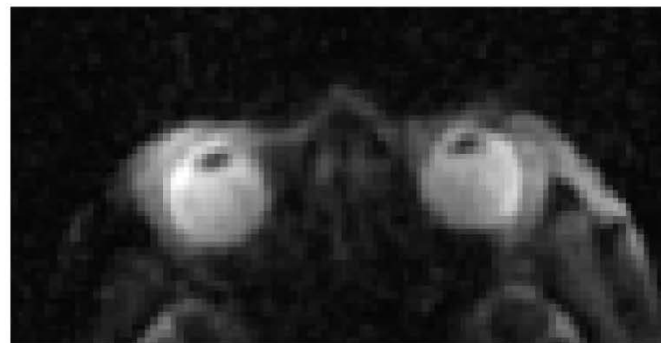
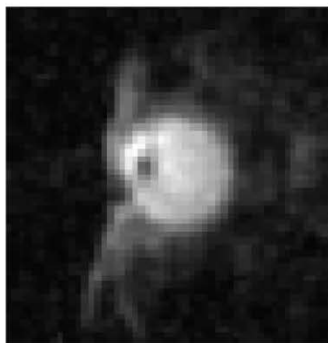
sagittal

axial

Supporting Figure S1

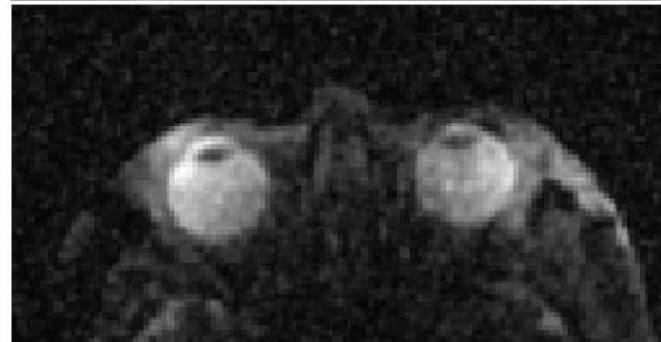
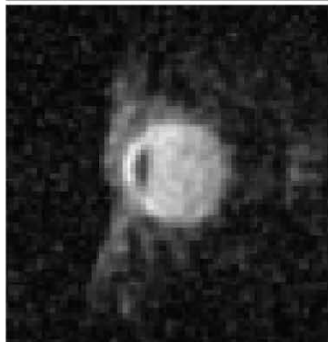
^{23}Na image
(1.4 x 1.4 x 1.4)
 mm^3

10 min 50 s



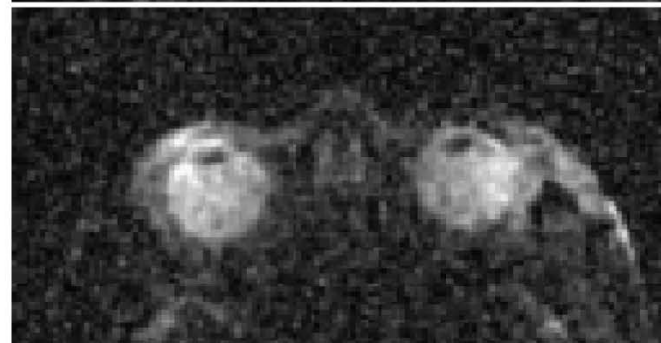
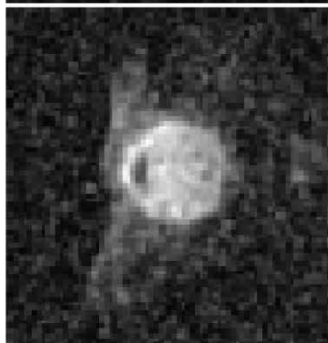
^{23}Na image
(1.0 x 1.0 x 1.0)
 mm^3

14 min 10 s



^{23}Na image
(1.0 x 1.0 x 1.0)
 mm^3

10 min 50 s



^1H image



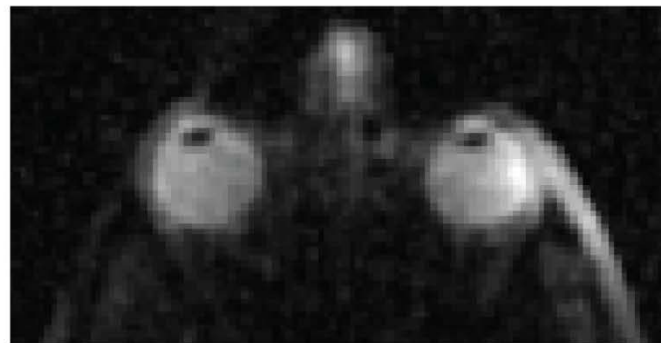
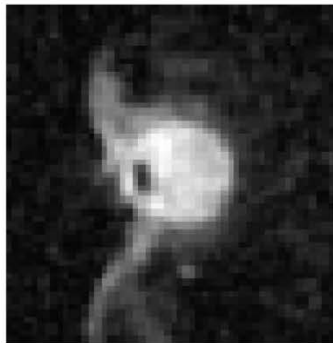
sagittal

axial

Supporting Figure S2

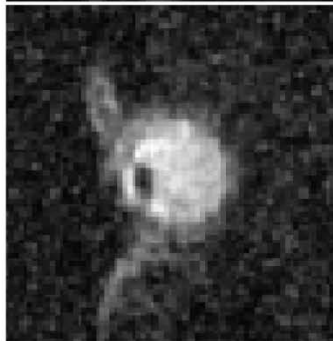
^{23}Na image
(1.4 x 1.4 x 1.4)
 mm^3

10 min 50 s



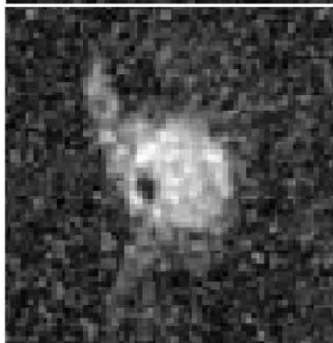
^{23}Na image
(1.0 x 1.0 x 1.0)
 mm^3

14 min 10 s



^{23}Na image
(1.0 x 1.0 x 1.0)
 mm^3

10 min 50 s



^1H image

